



Collisions of room-temperature helium with ultracold lithium and the van der Waals bound state of HeLi

Constantinos Makrides 

*Joint Quantum Institute, College Park, Maryland 20742, USA,
and Department of Physics, University of Maryland, College Park, Maryland 20742, USA*

Daniel S. Barker, James A. Fedchak, Julia Scherschligt , and Stephen Eckel
National Institute of Standards and Technology, Gaithersburg, Maryland 20899, USA

Eite Tiesinga 

*Joint Quantum Institute, College Park, Maryland 20742, USA;
Joint Center for Quantum Information and Computer Science, College Park, Maryland 20742, USA;
and National Institute of Standards and Technology, Gaithersburg, Maryland 20899, USA*



(Received 19 July 2019; published 6 January 2020)

We have computed the thermally averaged total, elastic rate coefficient for the collision of a room-temperature helium atom with an ultracold lithium atom. This rate coefficient has been computed as part of the characterization of a cold-atom vacuum sensor based on laser-cooled ${}^6\text{Li}$ or ${}^7\text{Li}$ atoms that will operate in the ultrahigh-vacuum ($p < 10^{-6}$ Pa) and extreme-high-vacuum ($p < 10^{-10}$ Pa) regimes. The analysis involves computing the $X^2\Sigma^+$ HeLi Born-Oppenheimer potential followed by the numerical solution of the relevant radial Schrödinger equation. The potential is computed using a single-reference-coupled-cluster electronic-structure method with basis sets of different completeness in order to characterize our uncertainty budget. We predict that the rate coefficient for a 300 K helium gas and a 1 μK Li gas is $1.467(13) \times 10^{-9}$ cm^3/s for ${}^4\text{He} + {}^6\text{Li}$ and $1.471(13) \times 10^{-9}$ cm^3/s for ${}^4\text{He} + {}^7\text{Li}$, where the numbers in parentheses are the one-standard-deviation uncertainties in the last two significant digits. We quantify the temperature dependence as well. Finally, we evaluate the s -wave scattering length and binding of the single van der Waals bound state of HeLi. We predict that this weakly bound level has a binding energy of $-0.0064(43) \times hc$ cm^{-1} and $-0.0122(67) \times hc$ cm^{-1} for ${}^4\text{He}{}^6\text{Li}$ and ${}^4\text{He}{}^7\text{Li}$, respectively. The calculated binding energy of ${}^4\text{He}{}^7\text{Li}$ is consistent with the sole experimental determination.

DOI: [10.1103/PhysRevA.101.012702](https://doi.org/10.1103/PhysRevA.101.012702)

I. INTRODUCTION

The cold-atom vacuum standard (CAVS) shows promise in establishing an accurate primary pressure standard at room temperature in the ultrahigh-vacuum (UHV, $p < 10^{-6}$ Pa) and extreme-high-vacuum (XHV, $p < 10^{-10}$ Pa) regimes, where currently there are no reliable alternatives [1–4]. An operational CAVS device is expected to have fractional uncertainties in pressure readings of only several percentage points. In a CAVS device the pressure is proportional to the rate of atom loss of a small sample of ultracold alkali-metal sensor atoms from collisions with ambient atoms and molecules in the vacuum. Molecular hydrogen is the dominant unavoidable background constituent at our target pressures. Other constituents, e.g., He, N_2 , Ar, H_2O , CO_2 ,..., are either also unavoidable or deliberately added [2].

Rate coefficients for alkali-metal atoms colliding with these constituents will need to be determined either experimentally or theoretically. Our previous theoretical study regarding these collisions involved the determination of the loss-rate coefficient between lithium sensor atoms and molecular hydrogen, where lithium with its light mass is the most

promising candidate sensor atom [4]. This rate coefficient is predicted with a 2% one-standard-deviation uncertainty.

Comparisons of pressure measurements with the CAVS device to existing pressure standards at pressures larger than 10^{-6} Pa will validate the CAVS. In principle, this can be done by adding a known amount of any gas. A logical choice would be H_2 as the rate coefficients are already known. Helium is another natural candidate. It is a nonreactive gas and is often introduced as a way to help detect leaks in vacuum chambers.

In the CAVS device, a gas of ground-state lithium atoms is prepared at a temperature of ≈ 1 μK in a single hyperfine state. Lithium atoms will escape their trap, of depth approximately ten times their temperature, through collisions with helium atoms with near unit likelihood. We thus look to compute the energy-dependent total elastic cross section $\sigma(E)$ between ${}^4\text{He}$ and ${}^{6,7}\text{Li}$ as well as the thermally averaged rate coefficients $K(T_{\text{He}}, T_{\text{Li}})$, where E is the relative collision energy and T_{He} and T_{Li} are the helium and lithium gas temperatures, respectively.

Additionally, the HeLi dimer has been of interest for a number of years due to its unique single near-threshold bound state, useful for studies regarding three-body recombination

and absorption or adsorption of alkali-metal atoms on helium clusters of various sizes [5–7]. Since the 1970s many attempts have been made at computing the ground HeLi Born-Oppenheimer potential based on *ab initio* electronic structure methods [8–13]. More recently, this weakly bound state was experimentally observed; however, the experimental uncertainty was on the order of the binding energy with a central value that is an order of magnitude larger than the theoretical predictions [14]. We will also make a prediction for this binding energy, specifically focusing on the theoretical uncertainty. Finally, in anticipation of experiments where both dilute helium and lithium gasses are laser or evaporatively cooled and brought in contact, we present values for the so-called interspecies *s*-wave scattering length.

This paper is organized as follows. In Sec. II we present the *ab initio* $X^2\Sigma^+$ Born-Oppenheimer potential at different levels of accuracy within single-reference coupled-cluster theory. We also provide comparisons to two other determinations from the literature. Bound-state energies and radial wave functions of the ^4He $^6,7\text{Li}$ isotopologues are computed for each potential by numerically solving the relevant Schrödinger equation in Sec. III. Elastic cross sections and phase shifts are given in Sec. IV. The phase shifts are also compared to approximate semiclassical models. Section V characterizes the thermal rate coefficients. The values and uncertainties of the binding energy, the scattering length, and the helium-temperature-dependent parametrization of the thermalized rate coefficient are provided in Sec. VI. We conclude in Sec. VII.

II. POTENTIAL CURVES

The bound state and room-temperature collision between a lithium atom and a helium atom are dictated by the isotropic ground $X^2\Sigma^+$ adiabatic Born-Oppenheimer potential $V(R)$, where R is the interatomic separation between He and Li. Previously, this potential was computed in Refs. [9,11,13]. In this section, we construct two potentials from this data and describe our determination of this potential.

The first potential we consider is the analytical representation of the potential from Ref. [9] denoted here by $V^{\text{KTTY}}(R)$. The second potential $V^{\text{CSD}}(R)$ is constructed by combining the results from Refs. [11,13] with the long-range dispersion potential of Ref. [15]. Specifically, $V^{\text{CSD}}(R)$ contains the *ab initio* self-consistent-field (SCF) data from Ref. [13] for the repulsive inner wall with $R \in [3.0a_0, 8.0a_0]$, the post-SCF data from Ref. [11] for the potential well with $R \in (8.0a_0, 20.0a_0]$, and a dispersive form for $R > 20.0a_0$. The dispersion potential is written as

$$V^{\text{disp}}(R) = -C_6/R^6 - C_8/R^8 - C_{10}/R^{10}, \quad (1)$$

with the dispersion coefficients C_6 , C_8 , and C_{10} from Ref. [15]. Here $1a_0 = 0.0529177\dots$ nm is the Bohr radius. We ensure that the connection between each section is smooth and interpolate using a third-order Akima spline [16]. The dispersive form of the potential $V^{\text{KTTY}}(R)$ has coefficients that are within 0.2% of those of $V^{\text{CSD}}(R)$.

We additionally compute the $X^2\Sigma^+$ potential making use of modern *ab initio* electronic structure implementations. Our motivation for recomputing the potential energy curve

is our desire to place an uncertainty on binding energy and rate constants, which follows our experience in defining uncertainties for the $\text{Li} + \text{H}_2$ system in Ref. [4]. The $X^2\Sigma^+$ potential is computed using the coupled-cluster (CC) program of Kállay *et al.* [17] using unrestricted Hartree-Fock functions and correlating all five electrons at the coupled cluster with full single, double, and triple excitations (CCSDT) level of theory. The augmented, correlation consistent, polarized valence basis set aug-cc-pV x Z was used for helium, and the weighted-core variant aug-cc-pwCV x Z was used for lithium, where the cardinal number $x = T, Q, \text{ or } 5$. For each cardinal number we correct for the basis set superposition error (BSSE) using the counterpoise-correction algorithm of Ref. [18]. Near the equilibrium separation this correction for the $x = 5$ potential is about one half of the splitting between the $x = Q$ and 5 potentials. For brevity, we use $V^{xZ}(R)$ to denote these corrected potentials, where $x = T, Q, \text{ and } 5$. We then extrapolate to the complete basis set (CBS) limit [19] using the functional form $V^{nZ} = V^{\infty Z} + Be^{-(n-1)} + Ce^{-(n-1)^2}$ at each R , where $n = 3, 4, \text{ or } 5$ for the cardinal number $x = Q, T, \text{ or } 5$, respectively. The $x = \infty$ case corresponds to the CBS extrapolated potential.

At $R = 20.0a_0$, each $V^{xZ}(R)$ is connected to $V^{\text{disp}}(R)$ using the same dispersion coefficients as used for the CSD potential. The potentials $V^{xZ}(R)$ for $x = T, Q, 5, \text{ and } \infty$, the dispersion coefficients, and the procedure to connect the two parts are given in Table I. We would like to note that the authors of Ref. [20] find that $C_6 = 22.44(2) E_h a_0^6$, where E_h is the Hartree energy and the value in the parentheses is the one-standard-deviation uncertainty for the last significant digit. This value of C_6 would improve the connections of the potentials at $R = 20a_0$; however, Ref. [20] does not provide values for the other dispersion coefficients. Hence, we opted to use the values from Ref. [15]. The difference does not affect our final uncertainty budget for the observables.

Figure 1 compares all potentials. The $V^{xZ}(R)$ potentials are indistinguishable for $R < 10.0a_0$ in Fig. 1(a). At fixed potential energy their inner turning points are smaller than those of $V^{\text{CSD}}(R)$ and $V^{\text{KTTY}}(R)$. Figure 1(b) focuses on the potential well, where its depth D_e is $D_e/hc \approx 1.5 \text{ cm}^{-1}$ or equivalently $D_e/k_B \approx 2.1 \text{ K}$, much less than the 300 K room-temperature collision energies. Here, h is Planck's constant, c is the speed of light in vacuum, and k_B is the Boltzmann constant. Moreover, we observe that D_e becomes diminishingly larger for $x = T, Q, 5, \text{ and } \infty$. The depth of the CSD and KTTY potentials agrees best with that of the $V^{QZ}(R)$ potential. Differences $\Delta V^{xZ}(R) \equiv V^{xZ}(R) - V^{\infty Z}(R)$ between the potentials are shown in Figs. 1(c) and 1(d) as functions of R . Around the potential minimum $R \approx 11.5a_0$, the potentials are found to be within $1 \times hc \text{ cm}^{-1}$ of one another. Table II enumerates D_e and equilibrium separation r_e for each of the potentials.

A motivation to recompute the potential with modern electronic structure methods is based on the observation that the CSD and KTTY potentials have different predictions for the shape of the repulsive inner wall. The authors who computed the KTTY potential focused on the description of the attractive part of the potential, while the inner wall of the CSD potential is only based on a SCF method. We only use the $V^{xZ}(R)$ potentials to characterize

TABLE I. Parameters of the $V^{xZ}(R)$ potentials. The top part of the table contains the counterpoise-corrected values of $V^{xZ}(R)/hc$ in units of cm^{-1} with $x = T, Q, 5,$ and ∞ for a discrete set of R between $3.0a_0$ and $20.0a_0$. The $V^{\infty Z}(R)$ potential is a complete basis set extrapolation from the other three potentials. The bottom part of the table contains the dispersion coefficients in atomic units taken from Ref. [15] and used for $R \geq 20.0a_0$. The same dispersion coefficients are used for all four potentials. We use a third-order Akima spline [16] to interpolate the potentials for $R < 20.0$ and ensure smoothness by adding points from the analytical dispersion potential starting from $R = 20.0a_0$. The relative difference between the dispersive potential and the computed but not shown $V^{\infty Z}(R)$ at $R = 20.0a_0$ is $(V^{\text{disp}} - V^{\infty Z})/|V^{\infty Z}| = -0.44\%$.

$3.0a_0 \leq R < 20.0a_0$				
$R(a_0)$	TZ	QZ	$5Z$	∞Z
3.0	3576.65	3530.93	3521.41	3515.95
3.5	2423.05	2390.32	2385.13	2382.19
4.0	1813.88	1791.27	1787.33	1785.09
5.0	927.626	917.100	914.116	912.389
6.0	393.027	386.687	384.699	383.546
7.0	143.505	139.981	138.588	137.776
8.0	45.4608	43.6096	42.8019	42.3305
9.0	11.6136	10.6269	10.2007	9.952069
10.0	1.36949	0.872811	0.634163	0.494666
10.5	-0.362180	-0.701191	-0.881184	-0.986539
11.0	-1.115934	-1.342014	-1.475021	-1.552971
11.5	-1.356918	-1.505578	-1.601378	-1.657581
12.0	-1.344700	-1.442236	-1.509158	-1.548444
12.5	-1.219903	-1.284685	-1.331307	-1.358688
13.0	-1.057361	-1.101349	-1.132562	-1.150891
13.5	-0.893477	-0.923978	-0.944840	-0.957087
14.0	-0.744006	-0.765941	-0.779854	-0.788014
14.5	-0.615025	-0.631148	-0.640523	-0.646016
15.0	-0.506991	-0.518992	-0.525419	-0.529182
16.0	-0.345690	-0.352037	-0.355191	-0.357036
17.0	-0.238559	-0.241875	-0.243513	-0.244471
18.0	-0.167477	-0.169103	-0.170051	-0.170607
19.0	-0.119673	-0.120402	-0.120922	-0.121227
$R \geq 20.0a_0$				
C_6	$22.535 E_h a_0^6$			
C_8	$1084.2 E_h a_0^8$			
C_{10}	$72665.0 E_h a_0^{10}$			

the uncertainties in the binding energy and thermalized rate coefficients.

III. BOUND STATE OF HeLi

Rovibrational bound states of an isotropic potential are determined from the radial solutions $u_\ell(R)$ of the single-channel Schrödinger equation

$$\frac{d^2 u_\ell(R)}{dR^2} + \left[k^2 - \frac{\ell(\ell+1)}{R^2} - \frac{2\mu}{\hbar^2} V(R) \right] u_\ell(R) = 0, \quad (2)$$

where ℓ is the orbital angular momentum, μ is the reduced atomic mass for the ${}^4\text{He} + {}^{6,7}\text{Li}$ system, and \hbar is the reduced Planck constant. The potential operator $V(R)$ is the $X^1\Sigma^+$ Born-Oppenheimer potential determined in the previous

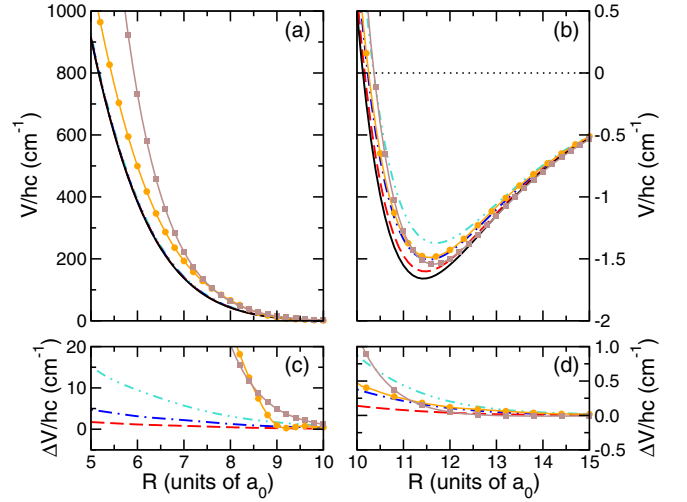


FIG. 1. Potential energy curves of the ground $X^2\Sigma^+$ state of HeLi as functions of the internuclear separation R . In all panels, the turquoise (double-dot-dashed), blue (dot-dashed), red (dashed), and black (solid) curves represent our CC potentials $V^{xZ}(R)$, with $x = T, Q, 5,$ and ∞ , respectively. The CSD and KTTY potentials obtained from the literature are represented by the brown curve with square markers and the orange curve with circle markers, respectively. (a) Comparison of the repulsive wall of the six potentials. The four $V^{xZ}(R)$ potentials are indistinguishable on this scale. (b) The attractive part of the potentials. Note that the vertical scale is 3 orders of magnitude smaller than that in panel (a). The zero of energy in both panels corresponds to the dissociation limit. Panels (c) and (d) show differences in potential energy with respect to the $V^{\infty Z}(R)$ potential for separations as in panels (a) and (b), respectively.

section and approaches zero as $R \rightarrow \infty$. The relative wave number k is defined through $E = \hbar^2 k^2 / 2\mu$, where E is the collision energy.

We compute the bound-state energies and radial wave functions for each of the potentials $V^X(R)$, where $X = TZ, QZ, 5Z, \infty Z, \text{CSD},$ and KTTY . We discretize the kinetic energy operator $-d^2/dR^2$ using the discrete variable representation (DVR) approach from Ref. [21] and solve the resulting matrix eigenvalue problem using LAPACK [22]. The radial grid is chosen carefully in anticipation of the rather large extent of the unit-normalized bound-state wave functions. We include R up to $6000a_0$ and are able to reproduce the bound-state energies of the KTTY potential for both isotopologues to the four significant digits given by Ref. [9].

We find that the potentials have only a single bound state with binding energy E_0 . It occurs for the $\ell = 0$ partial wave or the rotational quantum number. Table II lists E_0 and the expected size of the wave function $\langle R \rangle$ for each of the potentials and ${}^4\text{He} {}^6,7\text{Li}$ isotopologues. The bound-state energy is lower for deeper potentials. In fact, for the ${}^4\text{He} {}^7\text{Li}$ isotopologue the absolute value of $E_0^{\infty Z}$ is 12 times larger than $|E_0^{TZ}|$. Similarly, $\langle R \rangle$ decreases by a factor of 2. This behavior is even more dramatic for the ${}^4\text{He} {}^6\text{Li}$ isotopologue. Figure 2 compares the ${}^4\text{He} {}^7\text{Li}$ bound-state radial wave functions for the six potentials. They have a single maximum around $R \approx 20.0a_0$ and then gradually decrease to 0. More weakly bound states have more diffuse wave functions. The expected size $\langle R \rangle$ is also shown.

TABLE II. Selected spectroscopic and collisional properties of seven $X^2\Sigma^+$ HeLi potentials, with the CC- ∞Z entry being our most accurate determination. For each potential we present the equilibrium separation r_e and the depth of the potential D_e . The binding energy of the sole bound state E_0 , the expected size $\langle R \rangle$ of this bound state's wave function, and the cross section σ_{RT} at collision energy $E = E_{RT} = k_B \times 300$ K are shown for the two isotopologues ${}^4\text{He}$ ${}^6,7\text{Li}$. The energies D_e and E_0 are with respect to the atomization limit.

Potential	r_e (a_0)	D_e/hc (cm^{-1})	${}^4\text{He } {}^6\text{Li}$			${}^4\text{He } {}^7\text{Li}$		
			E_0/hc (cm^{-1})	$\langle R \rangle$ (a_0)	σ_{RT} (a_0^2)	E_0/hc (cm^{-1})	$\langle R \rangle$ (a_0)	σ_{RT} (a_0^2)
KTTY	11.64	1.543	-0.001 053	91.71	494.3	-0.003 907	53.20	496.7
CSD	11.55	1.489	-0.000 766	105.0	478.1	-0.003 299	56.62	480.1
CC- TZ	11.71	1.372	-0.000 098	267.6	478.7	-0.001 487	77.60	481.1
CC- QZ	11.54	1.506	-0.002 004	70.25	472.0	-0.005 539	46.76	474.4
CC- $5Z$	11.46	1.602	-0.004 429	51.66	469.1	-0.009 373	38.96	471.5
CC- ∞Z	11.42	1.661	-0.006 375	45.25	467.5	-0.012 199	35.72	469.9

IV. CROSS SECTIONS AND PHASE SHIFTS

The scattering length and cross sections are determined from numerical scattering state solutions of Eq. (2). Our numerical solver follows the propagator method of Johnson [23]. Namely, for each ℓ and E we propagate the logarithmic derivative of the wave function to sufficiently large R with a variable step size that adjusts according to changes in the solutions. Phase shifts $\eta_\ell(E)$ are extracted by matching to free-particle solutions and used to determine the s -wave or $\ell = 0$ scattering length $a^X = -\tan \eta_{\ell=0}^X(E)/k$ in the limit of $E \rightarrow 0$ and combined to form total cross sections

$$\sigma^X(E) = \frac{4\pi}{k^2} \sum_{\ell=0}^{\ell_{\text{MAX}}} (2\ell + 1) \sin^2 \eta_\ell^X(E), \quad (3)$$

where the superscript X is one of TZ , QZ , $5Z$, ∞Z , KTTY, or CSD and identifies the potential $V^X(E)$ used to com-

pute $\eta_\ell(E)$. Formally, $\ell_{\text{MAX}} = \infty$; However, sufficient convergence in $\sigma^X(E)$ is reached with $\ell_{\text{MAX}} = 200$ for our energy domain $0 < E \leq k_B \times 3000$ K. In essence, changes in $\sigma(E)$ from the cutoff in the summation over ℓ are much less than those among the potentials. The rather large energy domain relative to room temperature is motivated by convergence requirements for thermalized rate coefficients.

Figure 3 shows cross sections as functions of collision energy between 0 and $k_B \times 3000$ K for the potentials described in Sec. II. The cross sections are monotonically decreasing functions of energy. Due to the fact that the potentials are shallow and contain only a single bound state, we do not observe shape resonances. The nearly identical $V^{xZ}(R)$ potentials with $x = T, Q, 5$, and ∞ produce nearly identical $\sigma^{xZ}(E)$ with a progression to smaller cross sections with increasing cardinal number x . Interestingly, $\sigma^{\text{KTTY}}(E)$ is significantly larger than our *ab initio* $\sigma^{xZ}(E)$, but functionally similar. The cross section from $V^{\text{CSD}}(R)$ has a different functional form. Differences in the cross sections are due to the different

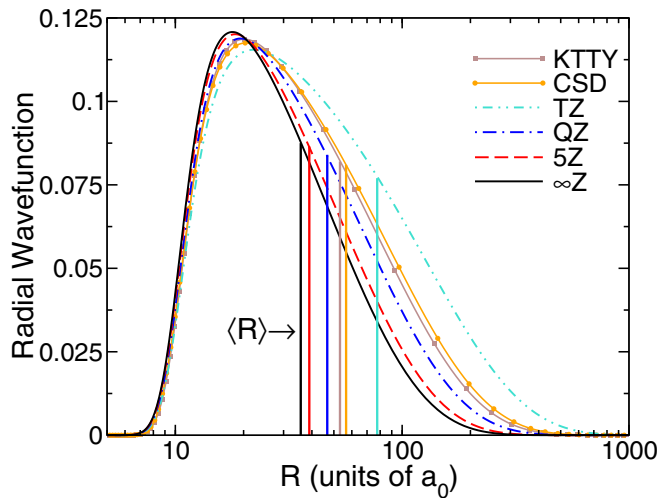


FIG. 2. Radial wave functions of the ${}^4\text{He}{}^7\text{Li}$ bound state as functions of the internuclear separation R . The x axis is on a logarithmic scale. The turquoise (double-dot-dashed), blue (dot-dashed), red (dashed), and black (solid) lines are for the $V^{xZ}(R)$ potentials with $x = T, Q, 5$, and ∞ , respectively. Wave functions for the CSD and KTTY potentials are shown by a brown curve with square markers and an orange curve with circle markers, respectively. The vertical solid lines with corresponding colors are the expected wave-function sizes $\langle R \rangle$.

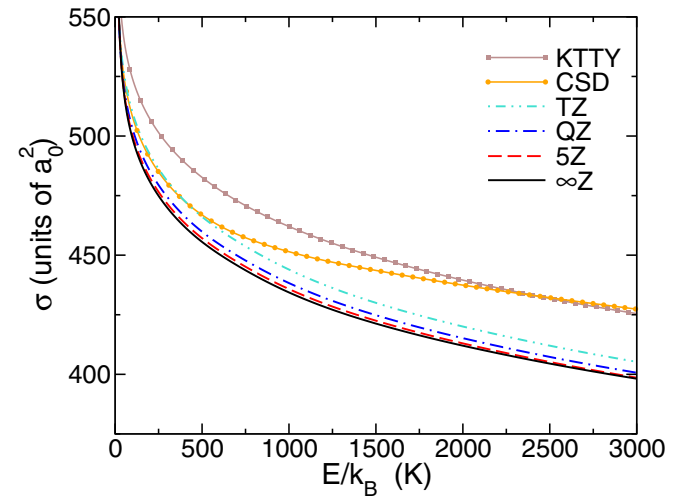


FIG. 3. Cross sections for ${}^4\text{He} + {}^7\text{Li}$ collisions, $\sigma(E)$, as functions of the collision energy E . The turquoise (double-dot-dashed), blue (dot-dashed), red (dashed), and black (solid) lines are cross sections based on our CC potentials $V^{xZ}(R)$ with $x = T, Q, 5$, and ∞ , respectively. The results for the CSD and KTTY potentials taken from the literature are shown as the brown curve with square markers and the orange curve with circle markers, respectively.

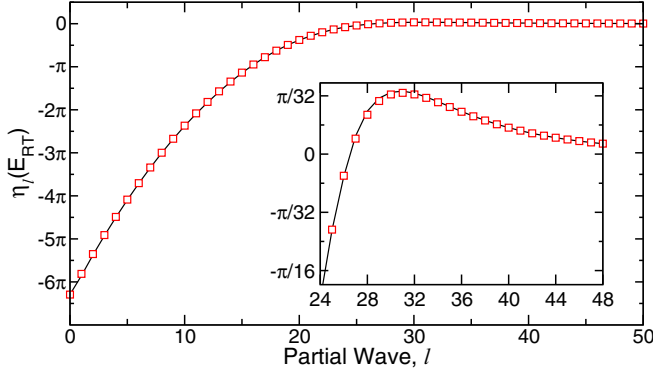


FIG. 4. Phase shifts $\eta_\ell(E_{RT})$ as functions of the partial wave ℓ for ${}^4\text{He} + {}^6\text{Li}$ at collision energy $E = E_{RT} = k_B \times 300$ K based on the $V^{\infty Z}(R)$ potential. The red square markers correspond to phase shifts obtained using coupled-channels calculations, while the solid black line corresponds to results based on a WKB approximation for $\eta_\ell(E)$. The two are indistinguishable on the scale of the figure. The inset is a blowup of the main panel.

repulsive walls of $V^X(R)$ for $R < 10.0a_0$. Our modern CC potentials provide a better description of this inner wall and thus provide more accurate cross sections.

It is worth noting that the semiclassical Wentzel-Kramers-Brillouin-Jeffreys (WKB) approximation for the phase shift is accurate for room-temperature collisions. Figure 4 shows phase shifts $\eta_\ell^{\infty Z}(E)$ as functions of ℓ at energy $E = E_{RT} = k_B \times 300$ K computed using the propagator method and the WKB approximation from Ref. [24]. The difference in $\eta_\ell(E)$ between the two approaches is at most 0.05π , largest at small partial waves. Furthermore, near the glory partial wave ℓ_G , defined as the partial wave where $\eta_\ell(E)$ is maximal, the difference is no more than $10^{-3}\pi$. For $E = E_{RT}$, $\ell_G = 31$. The cross sections determined from the propagator method and the WKB approximation agree to 0.42% at $E = E_{RT}$.

We observe that $\eta_\ell(E)$ from $\ell = \infty$ to ℓ_G does not go through a single π phase. This was also the case for $\text{Li} + \text{H}_2$ collisions at room temperature [4]. Consequently, the commonly used Born approximation for the phase shift based solely on the $1/R^6$ long-range dispersion potential

$$\eta_\ell^{\text{BA}}(E) = \frac{3\pi}{32} \left(\frac{E}{E_6} \right)^2 \frac{1}{\ell^5} \quad (4)$$

does not accurately approximate the total cross section. The contribution from the partial waves around ℓ_G cannot be ignored. Here, $E_6 = \hbar^2/2\mu\beta_6^2$ and $\beta_6 = (2\mu C_6/\hbar^2)^{1/4}$ are the energy and length scale associated with the van der Waals dispersion potential.

V. THERMALIZED RATE COEFFICIENTS

The thermalized rate coefficients $K(T_{\text{He}}, T_{\text{Li}})$ are found by integrating over Maxwell-Boltzmann distributions with He at temperature T_{He} and Li at temperature T_{Li} . This process reduces to a single integral over collision energy after

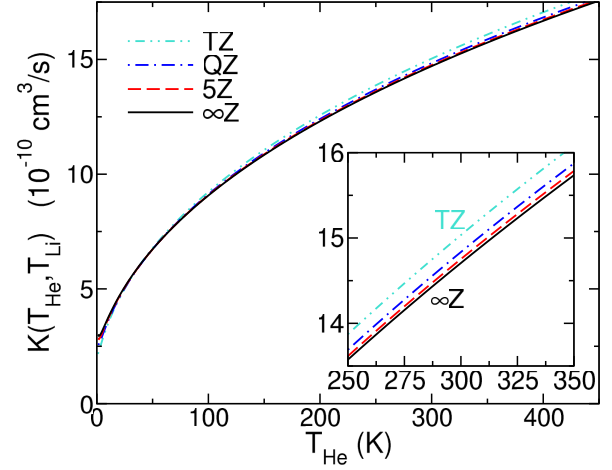


FIG. 5. Thermalized rate coefficients $K^{xZ}(T_{\text{He}}, T_{\text{Li}})$ as functions of the ${}^4\text{He}$ temperature T_{He} with ${}^7\text{Li}$ held at $T_{\text{Li}} = 1 \mu\text{K}$. The nearly overlapping turquoise (double-dot-dashed), blue (dot-dashed), red (dashed), and black (solid) lines are K^{xZ} with $x = T, Q, 5,$ and ∞ , respectively. The inset shows a blow-up of the region $250 \text{ K} \leq T_{\text{He}} \leq 350 \text{ K}$, where the differences in K^{xZ} can be better seen.

integrating out the center-of-mass motion. Specifically,

$$K(T_{\text{He}}, T_{\text{Li}}) = \frac{2}{\sqrt{\pi}} \sqrt{\frac{2k_B T_{\text{eff}}}{\mu}} \int_0^\infty d\zeta \zeta e^{-\zeta} \sigma(\zeta k_B T_{\text{eff}}), \quad (5)$$

where $\zeta = E/k_B T_{\text{eff}}$ and

$$T_{\text{eff}} = \frac{m_{\text{He}}}{m_{\text{Li}} + m_{\text{He}}} T_{\text{Li}} + \frac{m_{\text{Li}}}{m_{\text{Li}} + m_{\text{He}}} T_{\text{He}} \quad (6)$$

is an effective temperature.

The resulting $K(T_{\text{He}}, T_{\text{Li}})$ for the potentials $V^{xZ}(R)$ are shown in Fig. 5 as functions of T_{He} with $T_{\text{Li}} = 1 \mu\text{K}$. Near room temperature, the thermalized rate constants are functionally close to linear and are well represented by a Taylor expansion to second order in T_{He} around $T_{\text{RT}} = 300$ K and first order in T_{Li} around $1 \mu\text{K}$. Specifically,

$$K(T_{\text{He}}, T_{\text{Li}}) = \mathcal{K}_0 + \mathcal{K}_1 (T_{\text{He}} - T_{\text{RT}}) + \frac{1}{2} \mathcal{K}_2 (T_{\text{He}} - T_{\text{RT}})^2 + \frac{m_{\text{He}}}{m_{\text{Li}}} \mathcal{K}_1 (T_{\text{Li}} - 1 \mu\text{K}), \quad (7)$$

with expansion coefficients \mathcal{K}_i . The relationship between the expansion coefficients linear in $T_{\text{He}} - T_{\text{RT}}$ and $T_{\text{Li}} - 1 \mu\text{K}$ follows from the fact that the rate coefficient only depends on T_{eff} .

VI. UNCERTAINTY ANALYSIS OF BINDING ENERGY, SCATTERING LENGTH, AND RATE COEFFICIENTS

The largest source of uncertainty in the binding energy, the scattering length, and the thermalized rate coefficients comes from our inability to compute $V(R)$ exactly. The uncertainties from our numerical procedures in solving Eq. (2) are negligible in comparison. We quantify the uncertainties by first introducing the parametrization

$$V(R; \xi) \equiv V^{\infty Z}(R) + \xi W(R), \quad (8)$$

where $W(R) \equiv V^{QZ}(R) - V^{\infty Z}(R)$ and ξ is a dimensionless parameter. The potential $V(R; \xi)$ reasonably reproduces each of the $V^{xZ}(R)$ potentials with $\xi = 6.7, 1.0, 0.36,$ and 0.0 for $x = T, Q, 5,$ and ∞ , respectively. The decreasing changes in ξ in the progression of the cardinal number x from T to ∞ indicates convergence of the electronic structure calculations.

The value $\xi = \xi^{\infty Z} = 0.0$ is our best attempt at the true potential. We then treat ξ as a Gaussian-distributed random variable with mean $\xi^{\infty Z}$ and one-standard-deviation uncertainty $\sigma(\xi) = 1.0$, or equivalently the difference $|V^{QZ}(R) - V^{\infty Z}(R)|$ is the uncertainty of $V^{\infty Z}(R)$. We believe that this is a conservative estimate of the uncertainty and encompasses uncertainties from the BSSE and CBS extrapolations as well as those from small nonadiabatic recoil and relativistic corrections. In fact, nonadiabatic and relativistic corrections are expected to change the potential on the order of $(m_e/\mu)V(R)$ and $\alpha^2 V(R)$, respectively, where m_e is the mass of the electron and α is the fine-structure constant. These changes are much smaller than the energy difference between the QZ and ∞Z potentials.

In this framework the bound-state energy is then given by

$$E_0(\xi) = \mathcal{E}_0 + \mathcal{E}_1 \xi + O(\xi^2), \quad (9)$$

where \mathcal{E}_i are expansion coefficients. From the binding energies in Table II, we note that a linear expansion is sufficient for $\xi \leq 1$, but that higher orders of ξ are needed to account for the binding energy of the $V^{TZ}(R)$ potential, our least accurate potential. As this potential lies more than six standard deviations away from our best estimate of the potential, it does not effect our uncertainty analysis. From error propagation the one-standard-deviation uncertainty of the bound-state energy is then

$$\sigma(E_0) = \mathcal{E}_1 \sigma(\xi). \quad (10)$$

We have similarly determined the uncertainty of the s -wave or $\ell = 0$ scattering length $a(\xi) = a_0 + a_1 \xi + O(\xi^2)$ and $\sigma(a) = a_1 \sigma(\xi)$.

We also compute the uncertainty of the thermalized rate coefficients $K(T_{\text{He}}, T_{\text{Li}}; \xi)$. Expanding each of the expansion coefficients in Eq. (7) around $\xi = 0$, we have

$$\mathcal{K}_i(\xi) = \kappa_{i,0} + \kappa_{i,1} \xi, \quad (11)$$

where $\kappa_{i,j}$ are the expansion coefficients in ξ and $\mathcal{K}_i(0) = \kappa_{i,0} = \mathcal{K}_i^{\infty Z}$. Again through error propagation, we have

$$\sigma^2(K) = \sum_{i,j} \mathcal{K} \mathcal{K}_i \mathcal{K} \mathcal{K}_j r(\mathcal{K}_j, \mathcal{K}_j) \sigma(\mathcal{K}_i) \sigma(\mathcal{K}_j), \quad (12)$$

where the correlation coefficient between \mathcal{K}_j and \mathcal{K}_j is $r(\mathcal{K}_j, \mathcal{K}_j)$ and $\sigma(\mathcal{K}_i)$ are individual uncertainties. Since there is only a single random variable ξ that characterizes the distribution of the \mathcal{K}_i , we realize that $r(\mathcal{K}_j, \mathcal{K}_j) = 1$ and $\sigma(\mathcal{K}_i) = \kappa_{i,1} \sigma(\xi)$ from Eq. (11).

Our final values and uncertainties for the expansion coefficients \mathcal{K}_i , E_0 , and a are given in Table III. The expansion coefficients \mathcal{K}_i for the ${}^4\text{He}-{}^6\text{Li}$ and ${}^4\text{He}-{}^7\text{Li}$ collisions differ by less than their stated uncertainties. The equivalent differences for the binding energies and scattering lengths are larger but

TABLE III. (a) Predicted values and one-standard-deviation uncertainties for expansion coefficients \mathcal{K}_0 , \mathcal{K}_1 , and \mathcal{K}_2 of the thermalized total rate coefficient $K(T_{\text{He}}, T_{\text{Li}})$ as defined in Eq. (7) for near-room-temperature helium and $1 \mu\text{K}$ ${}^6,{}^7\text{Li}$ sensor atoms with $T_{\text{ref}} = 300 \text{ K}$. The uncertainty $\sigma(K)$ is found by error propagation with correlation coefficients $r(\mathcal{K}_i, \mathcal{K}_j) = 1$ when $i \neq j$. (b) Predicted values and one-standard-deviation uncertainties for the binding energy of the single bound state and the zero-collision-energy scattering length of the two isotopologues ${}^4\text{He}-{}^6,{}^7\text{Li}$. The experimental binding-energy data are from Ref. [14].

	\mathcal{K}_0 (cm^3/s)	\mathcal{K}_1 ($\text{cm}^3/\text{s/K}$)	\mathcal{K}_2 ($\text{cm}^3/\text{s/K}^2$)
(a)			
${}^4\text{He}-{}^6\text{Li}$	$1.467(13) \times 10^{-9}$	$2.155(23) \times 10^{-12}$	$-4.141(71) \times 10^{-15}$
${}^4\text{He}-{}^7\text{Li}$	$1.471(13) \times 10^{-9}$	$2.152(24) \times 10^{-12}$	$-4.131(76) \times 10^{-15}$
	E_0/hc (cm^{-1})		Scattering length
(b)	Theory	Experiment	(units of a_0)
${}^4\text{He}-{}^6\text{Li}$	$-0.64(43) \times 10^{-2}$		$+80(50)$
${}^4\text{He}-{}^7\text{Li}$	$-1.22(67) \times 10^{-2}$	$-2.4(2.5) \times 10^{-2}$	$+60(20)$

still their uncertainties overlap. These differences form an (over)estimate of the size of nonadiabatic corrections, where an electron is unable to follow its atom; i.e., the system seems to change its mass slightly during the collision. The change in the reduced mass μ based on ${}^6\text{Li}$ or ${}^7\text{Li}$ atoms is much larger.

Our prediction for the binding energy for the ${}^4\text{He}-{}^7\text{Li}$ isotopologue can be compared with the experimental determination in Ref. [14]. The values are consistent within the error bars. The relative uncertainty of the theoretical binding energy $\sigma(E_0)/|E_0| = 0.55$ is only a factor of 2 smaller than that of the experiment. Improving the theoretical accuracy will require improved and larger basis sets or including the complete configuration interaction. Such intensive computations fall outside the scope of our study.

The expansion in Eq. (7) with coefficients from Table III reproduces the rate coefficients for the $V^{\infty Z}(R)$ potential to 0.1% for $T_{\text{He}} \in [T_{\text{RT}} - 50 \text{ K}, T_{\text{RT}} + 50 \text{ K}]$ for both isotopologues. The dependence on the Li temperature up to $100 \mu\text{K}$ is negligible, but is included for completeness.

VII. CONCLUSIONS

We have determined total rate coefficients for the elastic scattering of lithium with helium near room temperature based on a calculation of the Li-He potential energy surface. We give rates for ${}^6\text{Li}$ and ${}^7\text{Li}$ colliding with ${}^4\text{He}$. The rate coefficients are important input parameters for the CAVS, a primary vacuum sensor operating in the UHV regime that is based on atom loss from a small sample of ultracold lithium atoms. We have carefully analyzed the uncertainty of our potential and been able to quote a fractional uncertainty for the rate coefficient of 1.0%. This accuracy is sufficient for the current goals of an operational CAVS. We have also given estimates of scattering lengths in the limit of zero collision energy and determined the binding energy of the only bound state in the Li-He potential. The latter is in agreement with the only experimental determination.

- [1] D. E. Fagnan, J. Wang, C. Zhu, P. Djuricanin, B. G. Klappauf, J. L. Booth, and K. W. Madison, *Phys. Rev. A* **80**, 022712 (2009).
- [2] J. Scherschligt, J. A. Fedchak, D. S. Barker, S. Eckel, N. Klimov, C. Makrides, and E. Tiesinga, *Metrologia* **54**, S125 (2017).
- [3] S. Eckel, D. S. Barker, J. A. Fedchak, N. N. Klimov, E. Norrgard, J. Scherschligt, C. Makrides, and E. Tiesinga, *Metrologia* **55**, S182 (2018).
- [4] C. Makrides, D. S. Barker, J. A. Fedchak, J. Scherschligt, S. Eckel, and E. Tiesinga, *Phys. Rev. A* **99**, 042704 (2019).
- [5] H. Suno and B. D. Esry, *Phys. Rev. A* **82**, 062521 (2010).
- [6] F. Stienkemeier, J. Higgins, W. E. Ernst, and G. Scoles, *Phys. Rev. Lett.* **74**, 3592 (1995).
- [7] B. Friedrich, *Physics* **6**, 42 (2013).
- [8] U. Kleinekathöfer, K. Tang, J. Toennies, and C. Yiu, *Chem. Phys. Lett.* **249**, 257 (1996).
- [9] U. Kleinekathöfer, M. Lewerenz, and M. Mladenović, *Phys. Rev. Lett.* **83**, 4717 (1999).
- [10] D. Cvetko, A. Lausi, A. Morgante, F. Tommasini, P. Cortona, and M. G. Dondi, *J. Chem. Phys.* **100**, 2052 (1994).
- [11] V. Staemmler, *Z. Phys. D* **39**, 121 (1997).
- [12] S. H. Patil, *J. Chem. Phys.* **94**, 8089 (1991).
- [13] E. Czuchaj, F. Reberntrost, H. Stoll, and H. Preuss, *Chem. Phys.* **196**, 37 (1995).
- [14] N. Tariq, N. A. Taisan, V. Singh, and J. D. Weinstein, *Phys. Rev. Lett.* **110**, 153201 (2013).
- [15] J. Jiang, J. Mitroy, Y. Cheng, and M. Bromley, *At. Data Nucl. Data Tables* **101**, 158 (2015).
- [16] H. Akima, *J. ACM* **17**, 589 (1970).
- [17] M. Kállay, Z. Rolik, J. Csontos, P. Nagy, G. Samu, D. Mester, J. Csóka, B. Szabó, I. Ladjánszki, L. Szegedy *et al.*, MRCC, a quantum chemical program suite, 2013.
- [18] S. Boys and F. Bernardi, *Mol. Phys.* **19**, 553 (1970).
- [19] M. P. de Lara-Castells, R. V. Krems, A. A. Buchachenko, G. Delgado-Barrio, and P. Villarreal, *J. Chem. Phys.* **115**, 10438 (2001).
- [20] A. Derevianko, S. G. Porsev, and J. F. Babb, *At. Data Nucl. Data Tables* **96**, 323 (2010).
- [21] D. T. Colbert and W. H. Miller, *J. Chem. Phys.* **96**, 1982 (1992).
- [22] E. Anderson, Z. Bai, C. Bischof, S. Blackford, J. Demmel, J. Dongarra, J. Du Croz, A. Greenbaum, S. Hammarling, A. McKenney *et al.*, *LAPACK Users' Guide*, 3rd ed. (Society for Industrial and Applied Mathematics, Philadelphia, PA, 1999).
- [23] B. Johnson, *J. Comput. Phys.* **13**, 445 (1973).
- [24] F. H. Mies and P. S. Julienne, *J. Chem. Phys.* **77**, 6162 (1982).